MATERIALS SCIENCE

Hybrid magnon-phonon localization enhances function near ferroic glassy states

Michael E. Manley[1]*, Paul J. Stonaha[1]†, Nickolaus M. Bruno[2,3], Ibrahim Karaman[2], Raymundo Arroyave[2], Songxue Chi[4], Douglas L. Abernathy[4], Matthew B. Stone[4], Yuri I. Chumlyakov[5], Jeffrey W. Lynn[6]

Ferroic materials on the verge of forming ferroic glasses exhibit heightened functionality that is often attributed to competing long- and short-range correlations. However, the physics underlying these enhancements is not well understood. The $Ni_{45}Co_5Mn_{36.6}In_{13.4}$ Heusler alloy is on the edge of forming both spin and strain glasses and exhibits its magnetic field–induced shape memory and large magnetocaloric effects, making it a candidate for multicaloric cooling applications. We show using neutron scattering that localized magnon-phonon hybrid modes, which are inherently spread across reciprocal space, act as a bridge between phonons and magnons and result in substantial magnetic field–induced shifts in the phonons, triple the caloric response, and alter phase stability. We attribute these modes to the localization of phonons and magnons by antiphase boundaries coupled to magnetic domains. Because the interplay between short- and long-range correlations is common near ferroic glassy states, our work provides general insights on how glassiness enhances function.

INTRODUCTION

Solid-state multicaloric cooling is undergoing a rapid expansion, driven by the discovery of better materials (*1*) and devices (*2*, *3*) and motivated by the urgent need for cleaner and more efficient technologies for combatting climate change. Magnetic shape memory alloys (MSMAs) are promising candidate materials for multicaloric cooling. MSMAs exhibit both ferromagnetic and ferroelastic order and undergo a first-order martensitic phase transformation (*4*, *5*) that can be reversed by temperature or magnetic field (*6*–*9*). MSMAs can be classified as either ferro- or metamagnetic shape memory alloys, depending on whether the martensite state of the material is ferromagnetic or ferri/antiferromagnetic, respectively. Typically, the transverse acoustic (TA_2) phonons propagating along [110] displays the so-called "premartensitic" behavior, in which, upon cooling between the Curie and martensitic temperatures, the phonon develops a local minimum in phonon energy at $q \approx \left[\frac{1}{3}\ \frac{1}{3}\ 0\right]$ or, in the case of a shape memory strain glass (STG), becomes overdamped (*10*). Ab initio calculations by Entel *et al.* (*11*) predict that an applied magnetic field can be used to stabilize the phonons of the austenite phase of Ni_2MnIn well below the martensite transformation temperature; the increased magnetic moment from the applied field stiffens the TA_2 phonon to a positive energy, stabilizing the phase. This helps explain the observed magnetic field–induced shape memory effect (*6*–*9*), as well as giant magnetic field induced strains in many other ferromagnetic shape memory alloys (*12*–*18*). Indirect support for the phonon stabilization mechanism can be found in a large phonon stiffening observed with magnetic ordering below the Curie temperature in an MSMA (*19*). This large phonon stiffening enhances the demagnetization entropy (*19*) and should also boost magnetocaloric (*20*, *21*), elastocaloric (*2*), and multicaloric (*1*, *22*) functions. The phonon stiffening occurs in many phonon branches but is most prominent in the transverse optic (TO) mode along [100], and the [110]-TA_2 phonon is involved in the martensitic phase transformation. However, the phonons most sensitive to the development of magnetic order are nowhere near the magnon dispersion curves, making it difficult to identify the coupling mechanism. Furthermore, to fully explain the magnetic shape memory effect, there is a need for direct measurements of the impact of applied magnetic fields on the phonons.

In this work, we perform neutron scattering measurements of the magnetic field and temperature dependence of the phonons and magnons in the cubic ($a = 5.98$ Å) Heusler alloy $Ni_{45}Co_5Mn_{36.6}In_{13.4}$. We confirm that phonons stiffen (shift to higher frequencies) with both applied magnetic fields and magnetic ordering below the Curie temperature, thus revealing a phonon stabilization mechanism similar to that proposed by Entel *et al.* (*11*). Furthermore, we discover a prominent flat (localized) extra band that develops below the magnetic ordering temperature. The extra band is neither a phonon nor a magnon but exhibits phonon-like behavior at high momentum transfers and magnon-like behavior at low momentum transfers, indicating a hybrid character. A feature with a similar intensity profile in the diffuse elastic scattering points to this hybrid band being localized by antiphase boundaries, which are known to have an altered magnetic state (*23*), affect magnetoelasticity (*24*), and frustrate long-range order leading to the formation of strain or spin glass states (*7*). Annealing the crystal to promote antiphase boundary formation and develop an STG state leads to a pronounced increase in the localized hybrid mode (HM) intensity and reveals that the intensity extends into the elastic line, indicating a continuum of slow dynamics characteristic of ferroic glasses. This hybrid localization acts as a bridge between the magnon branch and the phonon branches most sensitive to magnetism, providing a natural explanation for the additional magnon-phonon coupling (*19*), as well as enhanced magnetocaloric (*25*) and magnetic shape memory (*6*) functions.

[1]Materials Sciences and Technology Division, Oak Ridge National Lab, Oak Ridge, TN 37831, USA. [2]Department of Materials Science and Engineering, Texas A&M University, College Station, TX 77843, USA. [3]NASA Glenn Research Center, Cleveland, OH 44135, USA. [4]Neutron Scattering Division, Oak Ridge National Lab, Oak Ridge, TN 37831, USA. [5]Siberian Physical Technical Institute, Tomsk State University, Tomsk, Russia. [6]NIST Center for Neutron Research, National Institute of Standards and Technology, Gaithersburg, MD, 20899, USA.
*Corresponding author. Email: manleyme@ornl.gov
†Present address: Department of Physics, Lafayette College, Easton, PA 18042, USA.

RESULTS

Triple-axis inelastic neutron scattering as function of temperature and magnetic field

Figure 1 shows the strong temperature and magnetic field dependence of the TO phonons observed along **Q** = [3, 3, *L*] in single-crystal Heusler MSMA $Ni_{45}Co_5Mn_{36.6}In_{13.4}$. These triple-axis measurements were performed on both the HB3 spectrometer at the High Flux Isotope Reactor of Oak Ridge National Laboratory (ORNL) and the BT7 spectrometer at the National Institute of Standards and Technology (NIST) Center for Neutron Research (see Materials and Methods for details). To obtain good agreement for the fit phonon energies between the spectra measured on the two instruments, shown at two temperatures for HB3 in Fig. 1 (A and B), we carefully account for small spurious features in the background, slight differences in the resolution ellipsoid (Fig. 1C, inset), and damped mode coupling as shown in Fig. 1C (see the Supplementary Materials for details on these corrections and the damped mode coupling model). The fit results to the HB3 data are an update on the analysis in (*19*), while the BT7 data, which include all the magnetic field dependence, have not been used before. The temperature dependence of the TO phonon energy at the X-point follows the magnetic ordering behavior as the Curie temperature, $T_C = 400$ K, is approached and crossed (Fig. 1D). The zero-field results measured on both HB3 and BT7 are consistent with each other (black and blue symbols in Fig. 1D) and with our earlier work on this alloy (*19*). The correlation of the phonon energy with magnetic ordering strongly suggests that the X-point phonon is also likely to be sensitive to the application of magnetic field. The temperature dependence curve uniformly shifts to higher energy with increasing field (Fig. 1D). Furthermore, the shift with magnetic field starts rapidly below about 4 T and then appears to increase more gradually with further increases up to 10 T, as shown in Fig. 1E. The rise is more rapid at 300 K, where the largest shift occurs by 1 T, than at 400 K (near T_C), where the largest shift occurs by 4 T. Figure 1F shows the impact of magnetic field and temperature on the dispersion curve along **Q** = [3, 3, *L*]. While the temperature effect appears strongest at the X-point, the impact of the magnetic field is most pronounced at the gap in the phonon branch near $L = 0.4$. Furthermore, the overall effect of the field is to open the gap and flatten the lower section of the branch (Fig. 1F). The behavior suggests a strong dynamic interaction with magnons in this region near the zone boundary X-point. Yet, the normal magnons are known to be confined to near the zone center, or Γ-point, at these energies (*19*).

Time-of-flight inelastic neutron scattering as a function of temperature

To explore the interactions of the phonons and magnons more fully, we performed time-of-flight inelastic neutron scattering measurements on the same MSMA $Ni_{45}Co_5Mn_{36.6}In_{13.4}$ crystal above and below T_C using the wide Angular-Range Chopper Spectrometer (ARCS) instrument at the Spallation Neutron Source of ORNL (see Materials and Methods for details). Figure 2 shows that, when slicing the data along a perpendicular direction through the same

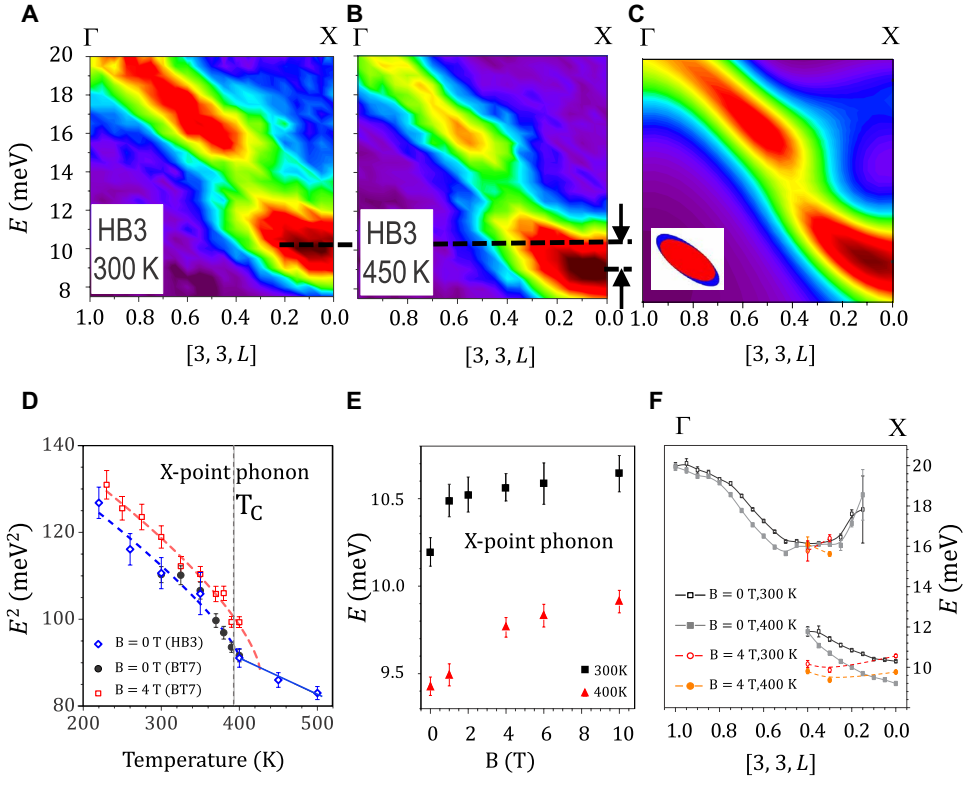

Fig. 1. Temperature and magnetic field dependence of the TO phonon near the X-point. (**A** and **B**) Spectral intensity maps of the TO phonon between the Γ- and X-points along **Q** = [3, 3, *L*] at 300 K [(A) below T_C] and 450 K [(B) above T_C]. (**C**) Spectral intensity map of coupled damped harmonic oscillator model convoluted with the instrument resolution ellipsoids shown in the inset (red for BT7 and blue for HB3). (**D**) Temperature dependence of the X-point phonon at 0 and 4 T. (**E**) Magnetic field dependence of the X-point phonon at 300 and 400 K. (**F**) Dispersion of TO phonon at 300 and 400 K with and without a 4-T field.

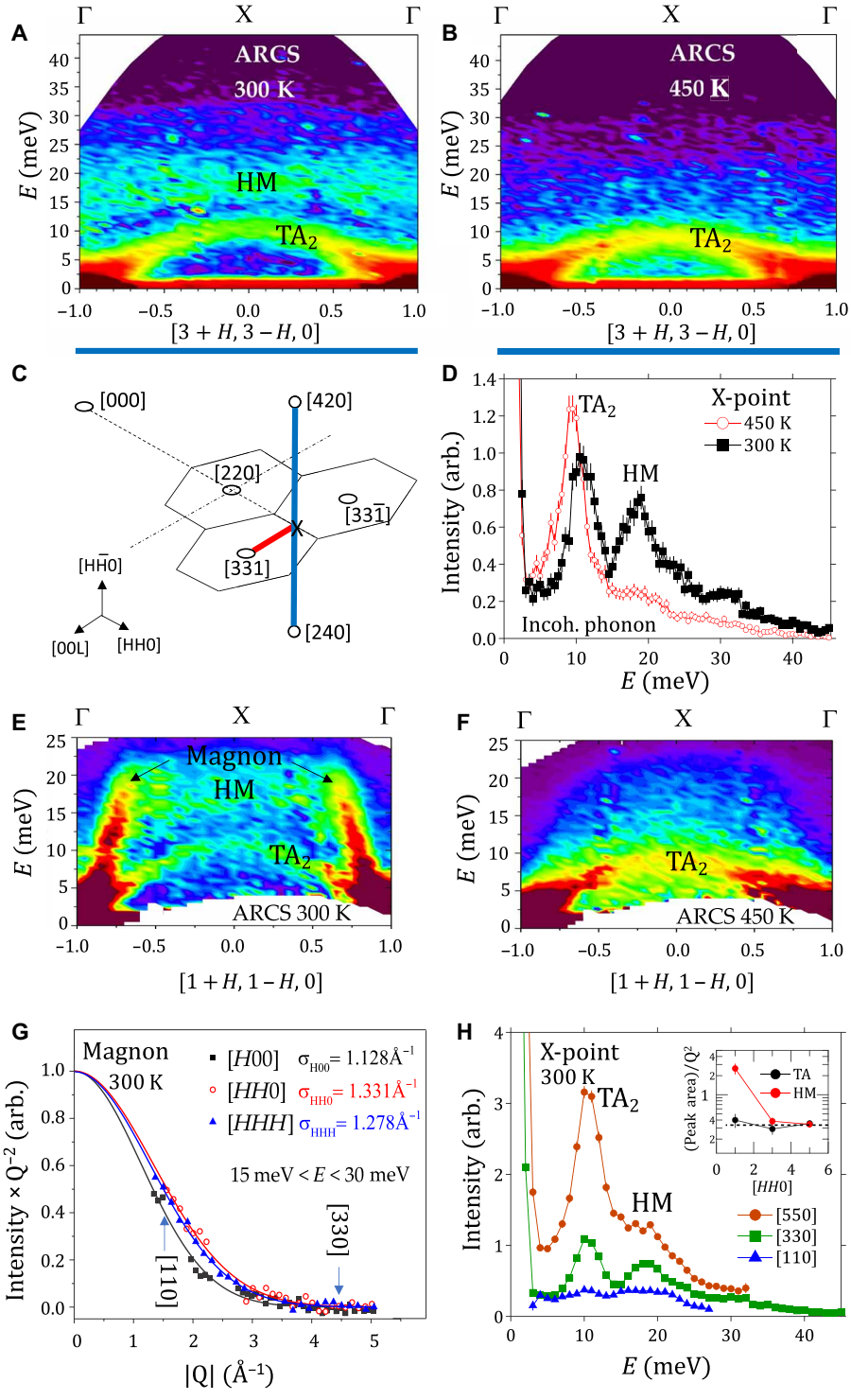

Fig. 2. Characterization of HMs that form in the inelastic spectrum above the TA_2 phonon at temperatures below the Curie temperature (T_C= 400 K). (**A** and **B**) Slices along **Q** = [3 + *H*, 3 − *H*, 0] below (300 K) and above (450 K) T_C, respectively. All slices are integrated in the perpendicular directions by ±0.1 reduced lattice units (r.l.u.). (**C**) Illustration of the relationship of the [3 + *H*, 3 − *H*, 0] direction (blue line) to the [3, 3, *L*] direction in Fig. 1 (red line), which cross the same X-point. (**D**) Cut through the X-point above and below T_C. (**E** and **F**) Slices along low-**Q** equivalent [1 + *H*, 1 − *H*, 0] direction, below (300 K) and above (450 K) T_C, respectively. (**G**) Magnetic form factor determined from magnon intensity. (**H**) Cuts at [5, 5, 0], [3, 3, 0], and [1, 1, 0] X-points. Inset shows the $|Q|^2$ normalized peak intensity dependence on [*H*, *H*, 0].

X-point as in Fig. 1, an additional dynamical feature appears below T_C. Comparing slices along $\mathbf{Q} = [3 + H, 3 - H, 0]$ in Fig. 2A at 300 K and Fig. 2B at 450 K, there is a pronounced broad nearly flat band of intensity at around 20 meV forming below $T_C = 400$ K that stretches across the zone just above the transverse acoustic (TA_2) phonon. This is the TA_2 phonon that exhibits "pre-martensitic" behavior in these shape memory alloys and is connected to the TO mode shown in Fig. 1 at the X-point; see illustration in Fig. 2C. The cut at the X-point in Fig. 2D shows that the band is comparable in intensity to the TA_2 phonon (there is also a background of incoherent phonon scattering due primarily to the incoherent cross sections of Co and Ni). Because this band appears with magnetic order, it should at least be associated with magnetism. However, at these high momentum transfers, the magnetic form factor suppresses magnetic scattering, being only ≈5% of its maximum (see Fig. 2G), so, here, the feature must be detected in the lattice dynamical motion at these values of **Q**, suggesting that it might be HMs, as indicated in Fig. 2.

To observe the same region with a much stronger magnetic and weaker phonon contribution requires examining the equivalent zones at lower momentum transfers. Figure 2 (E and F) shows the lower-**Q** equivalent of Fig. 2 (A and B) along $\mathbf{Q} = [1 + H, 1 - H, 0]$. In these data slices, the normal magnon dispersion curve, clearly observed near the Γ-points below T_C at 300 K (Fig. 3A), transitions to paramagnetic fluctuations above T_C at 450 K. The HM is also present but now appears to extend between the magnon dispersion curves above the TA_2 phonon in Fig. 2E. Figure 2G shows the magnetic form factor determined from the magnon intensities observed across multiple zones and directions. In this figure, the intensity is multiplied by the inverse magnitude squared of the momentum, $|Q|^{-2}$, because this results in phonon scattering intensities scaling as a constant. From Fig. 2G, the magnetic intensity is exponentially suppressed for momentum transfers at $\mathbf{Q} = [3, 3, 0]$ and above. Figure 2H shows cuts at three equivalent X-points [(5, 5, 0), (3, 3, 0), and (1, 1, 0)] that include both the TA_2 phonon and the HM. In going from (5, 5, 0) to (1, 1, 0), the TA_2 phonon peak area decreases by about a factor of 25, the expected $\mathbf{Q}^2$ dependence (*26*). Dividing out the $\mathbf{Q}^2$ dependence in the inset of Fig. 2H results in flat behavior for the TA_2. By contrast, the same analysis on the HM peak intensity divided by $\mathbf{Q}^2$, while flat at high Q (phonon-like), rises markedly at (1, 1, 0); see inset in Fig. 2H. This low-**Q** behavior is consistent with the magnetic form factor (Fig. 2G) and supports the idea that the extra band is a hybrid. To observe the HM in this phase at low temperatures, an STG state (*10*) of the alloy was prepared and measured on SEQUOIA at the Spallation Neutron Source of ORNL. These measurements show that the HM persists down to 5 K with the same high and low-**Q** dependence; see fig. S1. Figure S1 also shows that the HM appears in longitudinal scattering geometry along [00*L*].

To further explore the structure of the HM, magnons, and phonons in momentum space, we extract constant energy slices and cuts from the large volumes of ARCS data, as shown in Fig. 3. On the basis of our assessment of the magnetic form factor (Fig. 2G), the slice around the $\mathbf{Q} = [1, 1, 0]$ X-point in Fig. 3A is dominated primarily by magnetic scattering, while the slice around the $\mathbf{Q} = [5, 5, 0]$ X-phonon in Fig. 3B is dominated primarily by nuclear scattering. Hence, the constant energy slices provide relatively distinct color maps of the magnetic versus nuclear scattering intensities. From the primarily magnetic scattering in Fig. 3A, the HM extends broadly along $\mathbf{Q} = [1 + H, 1 - H, 0]$ between the magnons centered at (111) and $(11\bar{1})$, with a width in the perpendicular $\mathbf{Q} = [1, 1, L]$ direction of about 0.25 reduced lattice units. From the nuclear scattering in Fig. 3B, the HM appears as the intensity connecting the TO phonons in the perpendicular $\mathbf{Q} = [1, 1, L]$ direction. The cuts along $\mathbf{Q} = [1 + H, 1 - H, 0]$ in Fig. 3 (C and D) show the consistency of the HM when viewed in either the primarily magnetic scattering with the magnon (Fig. 3C) or the primarily nuclear scattering without the magnon (Fig. 3D); the HM intensity fits the same shape curve in both of these panels, which is fit using $\mathrm{sech}(2.2(H)^2)$ with a different scale factor and background level (the magnon peaks are fit to Gaussians). Hence, the HM reflects the same feature with both a magnetic and nuclear scattering component and connects the phonons and magnons crosswise in the zone.

The HM-mediated magnon-phonon coupling mechanism observed here (Fig. 3) is different than the way coupling usually manifests, either as an anti-crossing between existing phonons and magnons (*27*–*31*) or with the coupling of phonons to an existing two-magnon continuum (*32*). What the other mechanisms have in common is that they involve the mixing and/or rearrangements of phonon and magnon excitations dictated by the average structure. The HM appears to be an extra feature not associated with the known average lattice or magnetic structure (*19*), suggesting that it might originate with local deviations from the average crystal and magnetic structure. This would be consistent with the fact that the $Ni_{45}Co_5Mn_{36.6}In_{13.4}$ alloy exhibits degrees of local configurational order/disorder that can be used to stabilize both STGs and magnetic glasses (*7*, *33*, *34*), indicating that the local order/disorder strongly couples to both the lattice and magnetic properties. In addition, antiphase boundaries, which occur in $Ni_{45}Co_5Mn_{36.6}In_{13.4}$ alloys (*10*), are known to have a local magnetization state different from that of the matrix in other Heusler alloys (*23*, *35*) and alter bulk elastic properties (*24*, *36*). Such local order/disorder atomic displacements manifest as patterns of diffuse elastic scattering (*10*). Hence, to explore the relationship further, we next examine the diffuse elastic scattering.

The diffuse elastic scattering patterns shown in Fig. 4 confirm substantial local deviations (*7*) from the average crystal structure. Prominent features in the [*HHL*] scattering plane (Fig. 4A) include an alternating pattern of longitudinal diffuse intensity along [00*L*] emanating from the even-index Bragg reflections (see top inset in Fig. 4A); on the low $|\mathbf{Q}|$ side of the peak for $|H| + |K| + |L| = 4N$ and on the high $|\mathbf{Q}|$ side for $|H| + |K| + |L| = 4N + 2$, where N is an integer. The diffuse scattering also occurs along [*HHH*] and connects with the odd index reflections ($L2_1$ order), as indicated near the $(\overline{331})$ reflection in the bottom inset in Fig. 4A. These patterns are consistent with the two kinds of antiphase boundaries in Heusler structures, corresponding to displacement vectors $\mathbf{R} = {}^1/_2\langle 001\rangle$ and $\mathbf{R} = {}^1/_4\langle 111\rangle$ (*35*), and the coherence length along [00*L*] of $\xi = 1.1 \pm 0.2$ nm (Fig. 4B) is consistent with the 1.2-nm-thick antiphase boundary imaged by electron microscopy in (*10*). The HM intensity also appears in longitudinal scans extended along [00*L*], as shown in fig. S1. Figure 4C shows how the transverse diffuse scattering extends out of the plane in an orientation very close to the equivalent of the inelastic slices in Fig. 3 (the slice is offset to avoid an aluminum powder ring, bottom inset in Fig. 4A). That the bands of diffuse intensity share similarities with the localized HM intensity profiles (Fig. 3 and fig. S1) suggests that the HM is localized by the antiphase boundaries, causing the diffuse bands in this alloy (*10*).

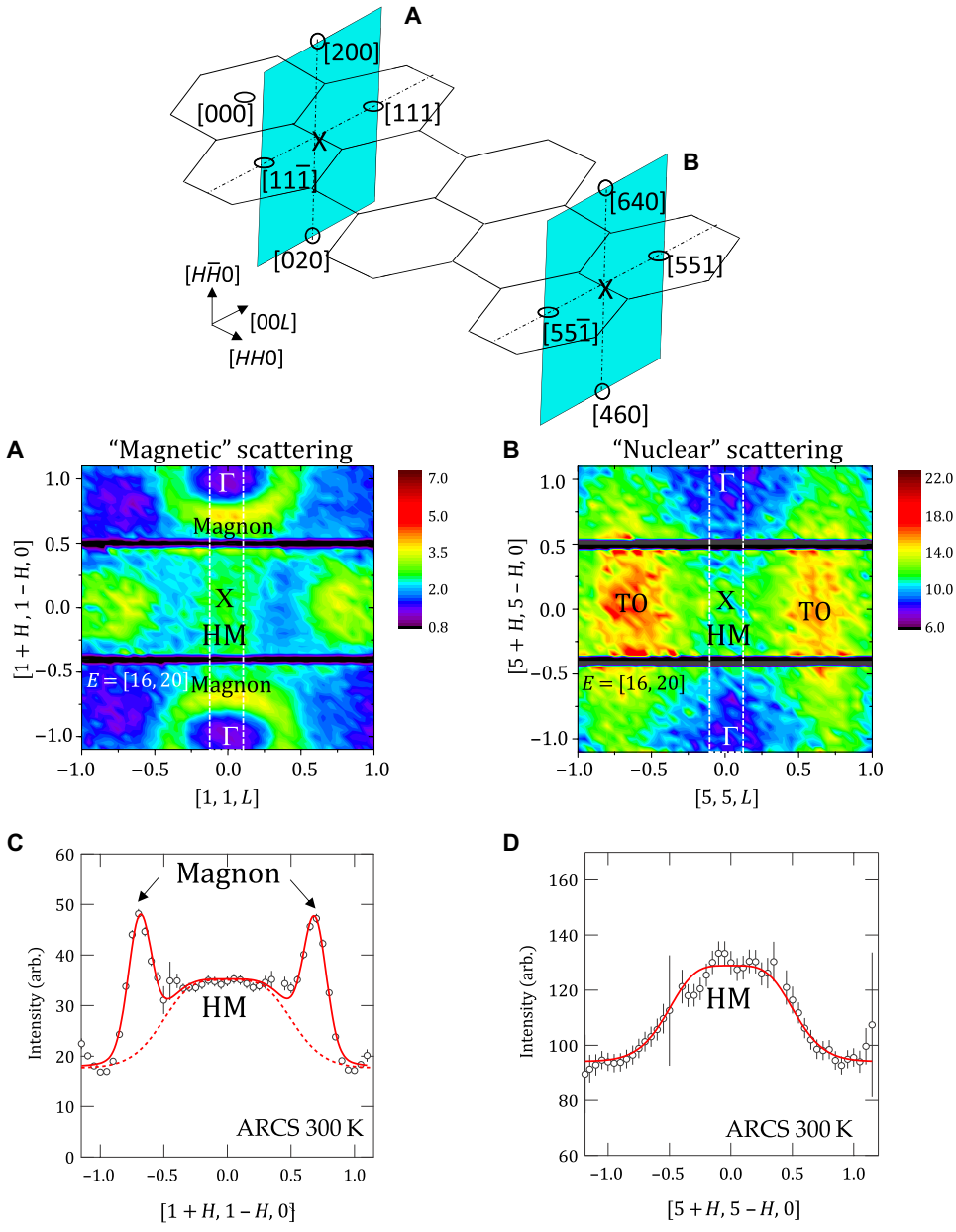

Fig. 3. Constant energy slices showing the momentum-space relationship between the HMs and the magnon and TO phonon. (**A** and **B**) Constant energy slices (E = [16, 20] meV) with primarily magnetic scattering near (110) X-point (A) and primarily nuclear scattering for near the (550) X-point (B) (see illustration at top for locations in reciprocal space). Slices are ±0.1-r.l.u. thick in the [HH0] direction. The dark horizontal lines near H = ±0.5 r. l. u. are from gaps in the detectors. A neutron absorption correction was applied to symmetrize image. (**C** and **D**) Cuts in the primarily magnetic scattering along [1 + H, 1 − H, 0] (C) and primarily nuclear scattering along [5 + H, 5 − H, 0] (D), indicated by vertical dashed lines in (A) and (B), respectively.

A connection between the HM and antiphase boundaries can be understood by considering the dynamics of a known interaction between fine magnetic domain walls and antiphase boundaries. For Ni-Mn-Ga MSMAs, it was shown that quenching in a high density of antiphase boundaries results in substantially enhanced elastic softening before the martensitic transformation (*24*). This elastic softening was attributed to the formation of fine magnetic domain patterns with domain walls pinned on antiphase boundaries, where the interaction of antiphase boundaries with domain walls amplifies the contribution of magnetostriction to elasticity (*24*). This provides a mechanism coupling the lattice to magnetism through the antiphase boundaries and should also enhance local variations in elastic stiffness on the scale of the antiphase boundaries [1.2 nm; see (*10*)]. Such small-scale variations in elasticity around the antiphase boundaries should also affect the lattice dynamics. First-principles phonon calculations in Fe_3Al with and without antiphase boundaries show that the presence of these boundaries results in elastic softening and a cluster of additional soft optic bands above the acoustic modes (*36*), just like where the HM intensity band is in Fig. 2A. In the calculation, however, the antiphase boundaries are spaced periodically,

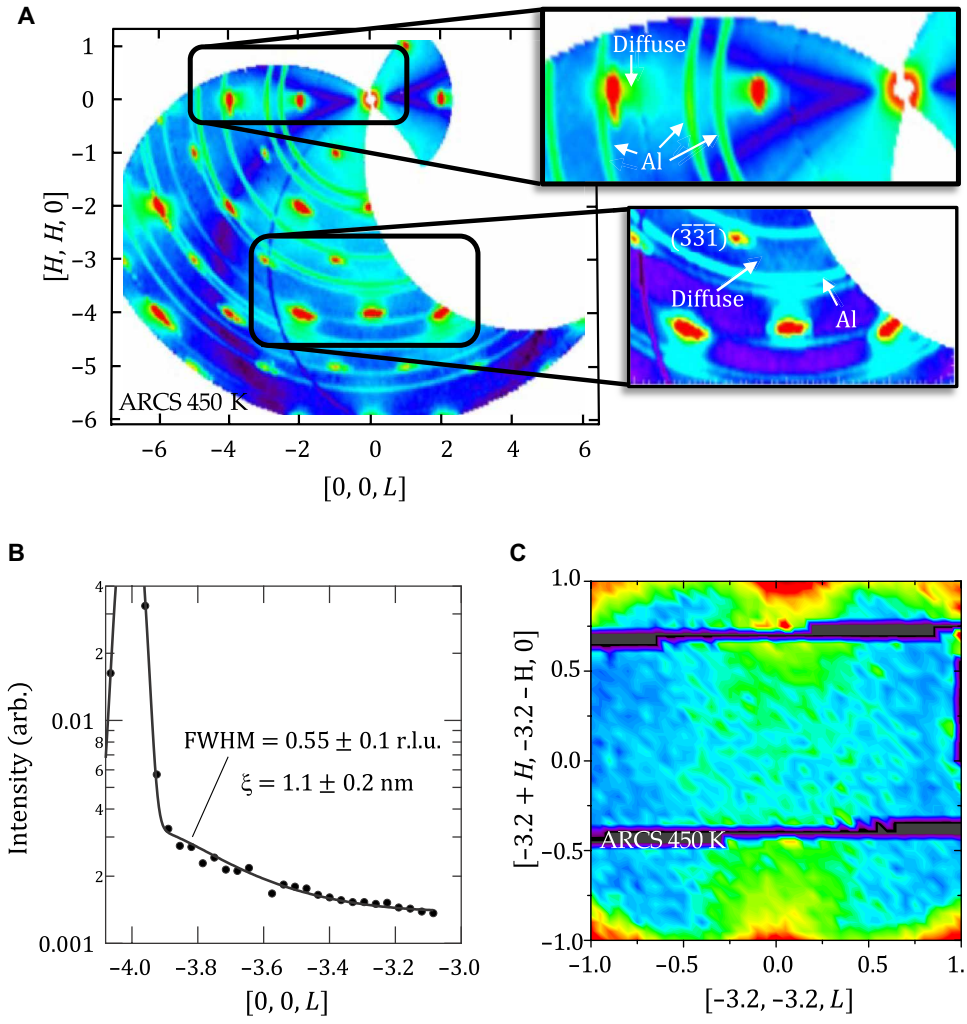

Fig. 4. Diffuse elastic neutron scattering measured on ARCS at 450 K, integrated over the energy range1 meV < *E* < 1 meV. (**A**) Prominent diffuse scattering in the form longitudinal bands along the [00*L*] direction emanating from the Bragg reflections and oscillating between positive and negative directions. The rings of intensity centered around zero are aluminum powder rings from crystal holder. The dark blue "shadows" emanating from zero and curving through the data are artifacts of neutron absorption with plate geometry. (**B**) Fit to the diffuse scattering along [00*L*] near the (00$\bar{4}$) reflection. The strong reflection is fit to a Gaussian, and the diffuse tail is fit to a broad Lorentzian with a full width at half maximum (FWHM) of 0.55 ± 0.2 r.l.u., indicating a coherence length of ξ = 1.1 ± 0.2 nm (using *a* = 5.98 Å). (**C**) Diffuse band of elastic intensity in transverse direction that is like the HM intensity profile.

resulting in distinct extra branches, while the real antiphase boundaries are more disordered. For a disordered arrangement, modes may become Anderson-localized (*37*–*39*) above some critical disorder strength and appear more diffuse in energy like the HM does (Fig. 2). Hence, we propose that the HM is a band of localized modes resulting from antiphase boundaries coupled to fine-scale magnetic domains below T_C. The HM then enhances the magnon-phonon coupling in the TO phonons at the energy of this band (Fig. 1) by bridging phonons and magnons (Figs. 2 and 3). Because annealing this MSMA promotes antiphase boundaries and STG formation (*7*), we next explore the impact of annealing this alloy into the STG state on the HM.

To directly compare the MSMA and STG states, a subset of the same $Ni_{45}Co_5Mn_{36.6}In_{13.4}$ crystals was annealed at 575 K for 3 hours to form the STG state and then measured using time-of-flight neutron scattering on the same ARCS instrument at the Spallation Neutron Source of ORNL (see Materials and Methods for details). Figure 5 compares the neutron scattering spectrum for the MSMA and STG states near the [332] and [112] X-points. As shown in Fig. 5A, the HM intensity for the STG spreads across the zone along Γ-X, much like in the MSMA (Fig. 2A). However, the cuts taken at the [332] X-point show that, relative to the TA_2 phonon peak, the HM intensity is about four times larger in the STG than in the MSMA. It is also clear that the HM intensity extends under the phonon peak and continues into the elastic line. Similarly, near the [112] X-point, where the magnetic cross section dominates, the HM appears as flat bands of intensity between the magnons (Fig. 5C), is several times more intense in the STG (Fig. 5D), and extends into the elastic line. These results confirm that the localized HMs are associated with increasing antiphase boundaries and STG formation. The substantial increase in the HM intensity compared to the relatively modest increases in the antiphase boundary concentration (*10*) points to a transition occurring at some critical concentration. The extension of the HM intensity into the elastic line indicates a continuum of slower dynamics, which is characteristic of ferroic glasses.

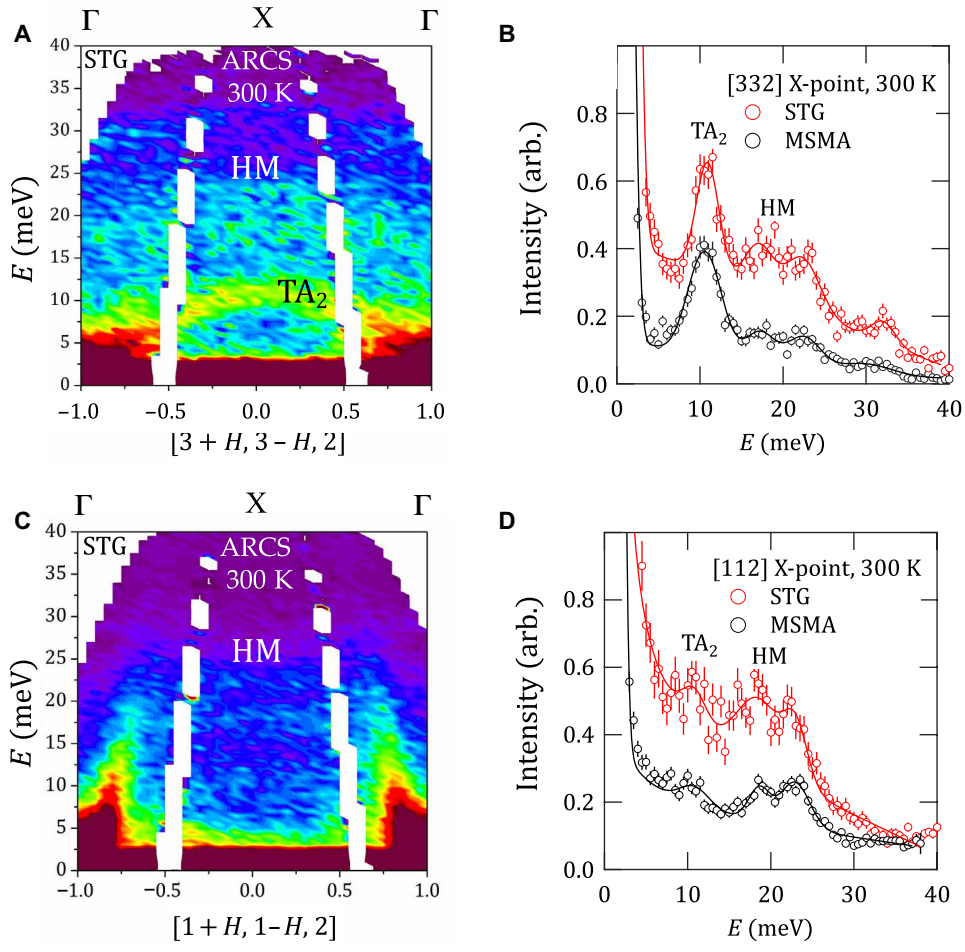

Fig. 5. Impact of the transition from MSMA to the STG state on the HMs. (**A**) Slice along **Q** = [3 + *H*, 3 − *H*, 2] in the STG state. (**B**) Cut through the [332] X-point in the STG and MSMA states. (**C**) Slice along **Q** = [1 + *H*, 1 − *H*, 2] in the STG state. (**D**) Cut through the [112] X-point in the STG and MSMA states. All slices and cuts are integrated in the unplotted reciprocal space directions by ±0.1 r.l.u. Error bars are statistical and represent one SD.

DISCUSSION

The dynamic coupling of the magnon and TO phonon via the HM influences functional properties in multiple ways. The magnetic field–induced shape memory effect (*6*), for example, occurs because magnetic fields stabilize the TA_2 phonon (*11*) near $q \approx \left[\frac{1}{3}\ \frac{1}{3}\ 0\right]$, and we observe that the HM-driven mechanism is associated with a stiffening (stabilization) of the TA_2 phonon near the zone boundary X-point at around 10 meV (Figs. 1 and 2). We cannot rule out that conventional coupling (*27*–*31*) at the magnon–TA phonon crossing (2- to 5-meV energy range; Fig. 2E) also acts to stiffen the lower part of the TA phonon branch; an anticrossing with the magnon would harden the TA phonon above the crossing. Crossing must occur because, at small wave vectors, the magnon is quadradic in the wave vector, while the acoustic phonon is linear. Thus, the HM-driven coupling mechanism probably works in concert with conventional coupling to control the magnetic shape memory effect by stabilizing the soft phonon. In the context of caloric effects, large shifts in the phonon density of states (DOS) with demagnetization have already been shown to make a substantial vibrational contribution to the demagnetization entropy (*19*), thereby enhancing the caloric response. The HM band itself is especially important to the caloric response because its large intensity (Fig. 2) clearly affects a large portion of the phonon DOS (*19*). Furthermore, the mixing of magnetic and elastic strain effects also lends itself to potentially more efficient magneto/elastocaloric cooling schemes where magnetic and mechanical stress fields are combined to obtain larger effects (*22*).

The impact of heat treating $Ni_{45}Co_5Mn_{36.6}In_{13.4}$ crystals on the latent heat of the martensitic transition was studied by Bruno *et al.* (*40*). In crossing from the shape memory alloy to the STG state, the latent heat of the martensitic transition increases from 2.3 kJ/kg to a peak of 7.7 kJ/kg just before the transition begins to partially arrest; see Fig. 6A. The associated extra entropy, determined by dividing the latent heat by the transition temperatures, amounts to 15.3 J/kg·K. This entropy can be explained, in large part, by the extra low-energy vibrational states in the STG compared to that in the MSMA (Fig. 5). To demonstrate this, we integrated our STG and MSMA phonon data over a common set of matching zones at high **Q** (to avoid magnetic scattering) and use this to generate neutron weighted phonon DOSs. From the shift in the phonon DOS, we estimate an extra vibrational entropy in the STG of 10.2 J/kg·K at the transition temperature (312 K), which accounts for about two-thirds of the total extra entropy. The remaining third likely comes from the magnetic degrees of freedom. The reference martensitic phases are

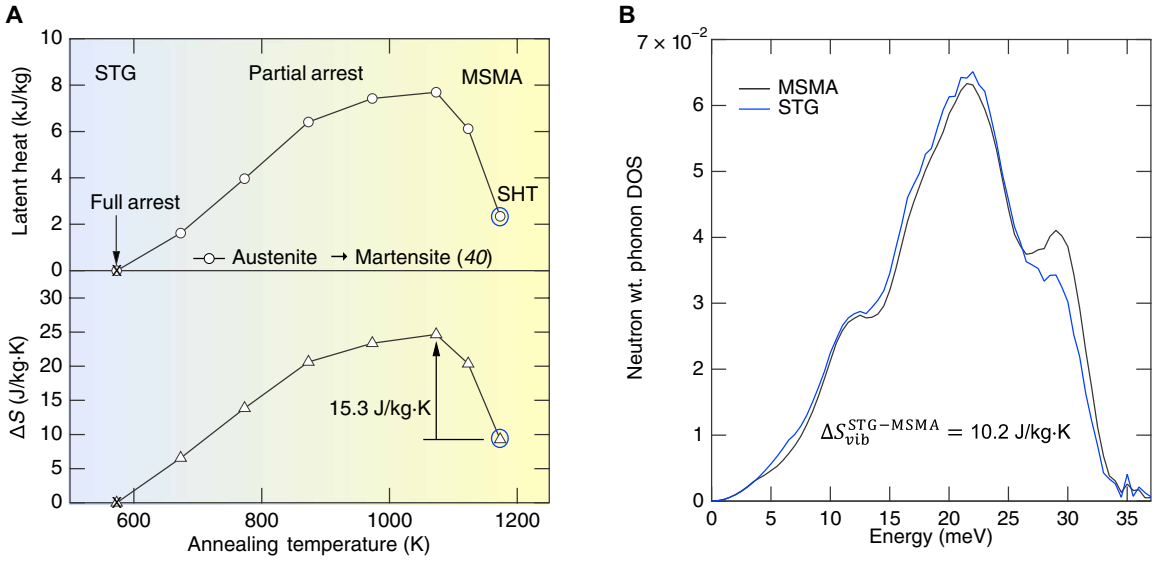

Fig. 6. Origin of enhanced caloric properties near the cross over from an MSMA to an STG. (**A**) Latent heat and entropy of the martensitic phase transition as a function of secondary annealing temperature, after Bruno *et al.* (*40*). The solution heat-treated (SHT) crystal is secondary annealed at progressively lower temperatures to promote STG formation. (**B**) Neutron weighted phonon DOS in STG and MSMA found by integrating neutron scattering data over a common set of zones at high **Q** (where magnetic scattering is negligible), correcting for multiphonon background, Debye-Waller factor, and thermal occupation factor. The in common **Q**-space integration range included [00*L*] = [−6, 2], [*HH*0] = [−2, −5] in the scattering plane, and [*K*, −*K*, 0] = [−1, 1] out of the scattering plane.

assumed to be relatively unaffected because the associated magnetoelastic softening vanishes below the transition (*24*).

The role played by local dynamics and structure in augmenting the functional responses in this MSMA parallels the way that polar nanoregions interact with long-range ferroelectric order in relaxor-based ferroelectrics, amplifying their giant electromechanical response (*41*–*43*). Despite the distinct ferroic order and nanoscale inhomogeneities, both systems are on the brink of disorder-frustrated ferroic states. The relaxor-based ferroelectric is on the verge of complete relaxor behavior, characterized by polar nanoregions. The MSMA is poised to adopt either a strain- or a spin-glass state depending on heat treatment (*7*). In both scenarios, local and long-range correlations vie for control over properties, culminating in heightened functionality. What sets our findings apart is the revelation that the interplay between long- and short-range correlations in the MSMA also actively orchestrates the strong coupling of magnetic and lattice degrees of freedom, thereby further enhancing its functional properties.

While the HMs observed here align well with previous calculations of an additional band of modes formed by a periodic arrangement of magnetically coupled antiphase boundaries (*36*), more realistic modeling that includes the randomness of the antiphase boundaries and related spin degrees of freedom is needed. Such calculations would likely provide additional insights into the development of ferroic glassy states and suggest more targeted strategies for optimizing functional properties for applications.

MATERIALS AND METHODS

Crystal growth

Single crystals of $Ni_{45}Co_5Mn_{36.6}In_{13.4}$ were grown using the Bridgman method in a high-purity He environment. The crystals were cut into nine thin strips (~30 mm by ~2 mm by 0.5 mm) with the long axis parallel to [1$\bar{1}$0] using wire electro-discharge machining (EDM). The brass layer that diffused into the sample during EDM was removed via mechanical polishing paper (800 to 1000 grit). Using x-ray diffraction, we verified the orientation of the single crystals from the [110] peak. The clean samples were then sandwiched within high-purity tantalum foil. The sandwiched samples were placed in a quartz vial and pulled to 0.01-mtorr vacuum at least three times to "scrub" the vial free of O_2. Between purges, the quartz vials were vented to 5 torr in high-purity Argon. The quartz vial was then sealed with a propane torch. The crystals were annealed at 1173 K for 24 hours to promote B2 atomic ordering and then quenched in water. The resulting Curie and martensitic transformation temperatures were $T_C = 400$ K and $T_M \approx 230$ K, respectively. This sample is referred to as the MSMA. Six of these crystals were aligned and laid into a flat-plate geometry (~30 mm by ~12 mm by 0.5 mm) for high-temperature neutron scattering measurements. The remaining three strips were wrapped in tantalum foil, reannealed at 573 K for 3 hours, and then quenched in water. We refer to these three pieces as the STG because the long-range martensitic phase transformation is arrested in these crystals (*10*), allowing measurements for the same average crystal structure down to low temperatures. These three crystals were aligned and laid into a flat-plate geometry in room temperature and below measurements.

Triple-axis inelastic neutron scattering

Parametric studies of the phonon dispersion as a function of temperature and magnetic field in the MSMA were performed using inelastic neutron scattering on two triple-axis spectrometers, the HB3 instrument (*44*) at the High Flux Isotope Reactor of ORNL and the BT7 instrument (*45*) at the NIST Center for Neutron Scattering at the NIST. Measurements on HB3 and BT7 focused on a region of momentum transfers (**Q**) around **Q** = [330], where anomalous phonon coupling to magnetic ordering was previously identified (*19*).

Measurements on both instruments covered a range of temperatures from as low as 200 K (undercooled) up to as high as 500 K, while the measurements on BT7 also included the application of a magnetic field up to $B = 10$ T. The measurements were made using a fixed final neutron energy of 14.7 meV and neutron collimations of 48′:50′:80′:120′ full width at half maximum. Analysis of the peak shapes and corrections for instrument background are described in more detail in the Supplementary Materials.

Time-of-flight inelastic neutron scattering

Comprehensive studies of the four-dimensional **Q**-E volume of phonon and magnon dispersion surfaces at different temperatures were performed using time-of-flight inelastic neutron scattering on two spectrometers, the ARCS (*46*) and SEQUOIA (*47*) instruments at the Spallation Neutron Source of ORNL. The ARCS measurements on the MSMA and STG were made using a fixed incident neutron energy of 50 meV. The MSMA was measured at 300 and 450 K (above and below $T_C = 400$ K in the high-temperature austinite phase of the MSMA), and the STG was measured at 300 K. To obtain a large **Q**-E volume, the crystal [001]-axis was rotated with respect to the incident beam from 40° to 125° collecting data at every 1° step. The SEQUOIA measurements were performed at 5 K on the STG with an incident neutron energy of 75 meV. To obtain a large volume, the crystal [001]-axis was rotated with respect to the incident beam collecting data from −10° to 150° in 1° steps.

Supplementary Materials

This PDF file includes:

Supplementary Text
Fig. S1
References

REFERENCES AND NOTES

1. H. Hou, S. Qian, I. Takeuchi, Materials, physics and systems for multicaloric cooling. *Nat. Rev. Mater.* **7**, 633–652 (2022).
2. S. Qian, D. Catalini, J. Muehlbauer, B. Liu, H. Mevada, H. Hou, Y. Hwang, R. Radermacher, I. Takeuchi, High-performance multimode elastocaloric cooling system. *Science* **380**, 722–727 (2023).
3. J. Li, A. Torelló, V. Kovacova, U. Prah, A. Aravindhan, T. Granzow, T. Usui, S. Hirose, E. Defay, High cooling performance in a double-loop electrocaloric heat pump. *Science* **382**, 801–805 (2023).
4. T. Hickel, M. Uijttewaal, A. al-Zubi, B. Dutta, B. Grabowski, J. Neugebauer, Ab initio-based prediction of phase diagrams: Application to magnetic shape memory alloys. *Adv. Eng. Mater.* **14**, 547–561 (2012).
5. M. Stipcich, L. Mañosa, A. Planes, M. Morin, J. Zarestky, T. Lograsso, C. Stassis, Elastic constants of Ni−Mn−Ga magnetic shape memory alloys. *Phys. Rev. B.* **70**, 054115 (2004).
6. R. Kainuma, Y. Imano, W. Ito, Y. Sutou, H. Morito, S. Okamoto, O. Kitakami, K. Oikawa, A. Fujita, T. Kanomata, K. Ishida, Magnetic-field-induced shape recovery by reverse phase transformation. *Nature* **439**, 957–960 (2006).
7. J. A. Monroe, J. E. Raymond, X. Xu, M. Nagasako, R. Kainuma, Y. I. Chumlyakov, R. Arroyave, I. Karaman, Multiple ferroic glasses via ordering. *Acta Mater.* **101**, 107–115 (2015).
8. Z. Li, C. Jing, H. L. Zhang, D. H. Yu, L. Chen, B. J. Kang, S. X. Cao, J. C. Zhang, A large and reproducible metamagnetic shape memory effect in polycrystalline $Ni_{45}Co_5Mn_{37}In_{13}$ Heusler alloy. *J. Appl. Phys.* **108**, 113908 (2010).
9. Y. Sutou, Y. Imano, N. Koeda, T. Omori, R. Kainuma, K. Ishida, K. Oikawa, Magnetic and martensitic transformations of NiMnX(X = In,Sn,Sb) ferromagnetic shape memory alloys. *Appl. Phys. Lett.* **85**, 4358–4360 (2004).
10. P. J. Stonaha, I. Karaman, R. Arroyave, D. Salas, N. M. Bruno, Y. Wang, M. F. Chisholm, S. Chi, D. L. Abernathy, Y. I. Chumlyakov, M. E. Manley, Glassy phonon heralds a strain glass state in a shape memory alloy. *Phys. Rev. Lett.* **120**, 245701 (2018).
11. P. Entel, M. E. Gruner, W. A. Adeagbo, A. T. Zayak, Magnetic-field-induced changes in magnetic shape memory alloys. *Mat. Sci. Eng. A* **481-482**, 258–261 (2008).
12. K. Ullakko, J. K. Huang, C. Kantner, R. C. O'Handley, V. V. Kokorin, Large magnetic-field-induced strains in Ni_2MnGa single crystals. *Appl. Phys. Lett.* **69**, 1966–1968 (1996).
13. A. Sozinov, A. A. Likhachev, N. Lanska, K. Ullakko, Giant magnetic-field-induced strain in NiMnGa seven-layered martensitic phase. *Appl. Phys. Lett.* **80**, 1746–1748 (2002).
14. T. Sakamoto, T. Fukuda, T. Kakeshita, T. Takeuchi, K. Kishio, Magnetic field-induced strain in iron-based ferromagnetic shape memory alloys. *J. Appl. Phys.* **93**, 8647–8649 (2003).
15. T. Wada, Y. Liang, H. Kato, T. Tagawa, M. Taya, T. Mori, Structural change and straining in Fe–Pd polycrystals by magnetic field. *Mater. Sci. Eng. A* **361**, 75–82 (2003).
16. T. Kakeshita, T. Takeuchi, T. Fukuda, M. Tsujiguchi, T. Saburi, R. Oshima, S. Muto, Giant magnetostriction in an ordered Fe_3Pt single crystal exhibiting a martensitic transformation. *Appl. Phys. Lett.* **77**, 1502–1504 (2000).
17. M. Wuttig, J. Li, C. Craciunescu, A new ferromagnetic shape memory alloy system. *Scr. Mater.* **44**, 2393–2397 (2001).
18. K. Oikawa, L. Wulff, T. Iijima, F. Gejima, T. Ohmori, A. Fujita, K. Fukamichi, R. Kainuma, K. Ishida, Promising ferromagnetic Ni–Co–Al shape memory alloy system. *Appl. Phys. Lett.* **79**, 3290–3292 (2001).
19. P. J. Stonaha, M. E. Manley, N. M. Bruno, I. Karaman, R. Arroyave, N. Singh, D. L. Abernathy, S. Chi, Lattice vibrations boost demagnetization entropy in a shape-memory alloy. *Phys. Rev. B.* **92**, 140406 (2015).
20. B. F. Yu, Q. Gao, B. Zhang, X. Z. Meng, Z. Chen, Review on research of room temperature magnetic refrigeration. *Int. J. Refrig.* **26**, 622–636 (2003).
21. V. K. Pecharsky, K. A. Gschneidner, Magnetocaloric effect and magnetic refrigeration. *J. Magn. Magn. Mater.* **200**, 44–56 (1999).
22. H. Hou, P. Finkel, M. Staruch, J. Cui, I. Takeuchi, Ultra-low-field magneto-elastocaloric cooling in a multiferroic composite device. *Nat. Commun.* **9**, 4075 (2018).
23. T. Tamaoka, R. Aso, Y. Murakami, Magnetism of antiphase boundaries in ordered alloys studied using electron holography. *J. Magn. Magn. Mater.* **539**, 168406 (2021).
24. H. Seiner, P. Sedlák, L. Bodnárová, J. Drahokoupil, V. Kopecký, J. Kopeček, M. Landa, O. Heczko, The effect of antiphase boundaries on the elastic properties of Ni–Mn–Ga austenite and premartensite. *J. Phys. Condens. Matter* **25**, 425402 (2013).
25. V. D. Buchelnikov, V. V. Sokolovskiy, M. A. Zagrebin, M. A. Tufatullina, P. Entel, First principles investigation of structural and magnetic properties of Ni-Co-Mn-In Heusler alloys. *J. Phys. D Appl. Phys.* **48**, 164005 (2015).
26. G. L. Squires, in *Introduction to the Theory of Thermal Neutron Scattering* (Cambridge Univ. Press, 2012), pp. 25–60.
27. S. Liu, A. Granados del Águila, D. Bhowmick, C. K. Gan, T. Thu Ha do, M. A. Prosnikov, D. Sedmidubský, Z. Sofer, P. C. M. Christianen, P. Sengupta, Q. Xiong, Direct observation of magnon-phonon strong coupling in two-dimensional antiferromagnet at high magnetic fields. *Phys. Rev. Lett.* **127**, 097401 (2021).
28. R. Takahashi, N. Nagaosa, Berry curvature in magnon-phonon hybrid systems. *Phys. Rev. Lett.* **117**, 217205 (2016).
29. G. Go, S. K. Kim, K.-J. Lee, Topological magnon-phonon hybrid excitations in two-dimensional ferromagnets with tunable chern numbers. *Phys. Rev. Lett.* **123**, 237207 (2019).
30. J. Cui, E. V. Boström, M. Ozerov, F. Wu, Q. Jiang, J. H. Chu, C. Li, F. Liu, X. Xu, A. Rubio, Q. Zhang, Chirality selective magnon-phonon hybridization and magnon-induced chiral phonons in a layered zigzag antiferromagnet. *Nat. Commun.* **14**, 3396 (2023).
31. B. Sheikhi, M. Kargarian, A. Langari, Hybrid topological magnon-phonon modes in ferromagnetic honeycomb and kagome lattices. *Phys. Rev. B.* **104**, 045139 (2021).
32. T. T. Mai, K. F. Garrity, A. McCreary, J. Argo, J. R. Simpson, V. Doan-Nguyen, R. V. Aguilar, A. R. H. Walker, Magnon-phonon hybridization in 2D antiferromagnet $MnPSe_3$. *Sci. Adv.* **7**, eabj3106 (2021).
33. W. Ito, M. Nagasako, R. Y. Umetsu, R. Kainuma, T. Kanomata, K. Ishida, Atomic ordering and magnetic properties in the $Ni_{45}Co_5Mn_{36.7}In_{13.3}$ metamagnetic shape memory alloy. *Appl. Phys. Lett.* **93**, 232503 (2008).
34. W. Ito, K. Ito, R. Y. Umetsu, R. Kainuma, K. Koyama, K. Watanabe, A. Fujita, K. Oikawa, K. Ishida, T. Kanomata, Kinetic arrest of martensitic transformation in the NiCoMnIn metamagnetic shape memory alloy. *Appl. Phys. Lett.* **92**, 021908 (2008).
35. S. P. Venkateswaran, N. T. Nuhfer, M. De Graef, Anti-phase boundaries and magnetic domain structures in Ni2MnGa-type Heusler alloys. *Acta Mater.* **55**, 2621–2636 (2007).
36. M. Friák, M. Černý, M. Šob, Temperature-dependent impact of antiphase boundaries on properties of Fe_3Al. *Intermetallics* **151**, 107746 (2022).
37. P. W. Anderson, Absence of diffusion in certain random lattices. *Phys. Rev.* **109**, 1492–1505 (1958).
38. A. Lagendijk, B. V. Tiggelen, D. S. Wiersma, Fifty years of Anderson localization. *Phys. Today* **62**, 24–29 (2009).
39. T. Yoshihiro, N. Nishiguchi, Mode-conversion effects of phonons on Anderson localization. *Phys. Rev. B* **100**, 235441 (2019).
40. N. M. Bruno, D. Salas, S. Wang, I. V. Roshchin, R. Santamarta, R. Arroyave, T. Duong, Y. I. Chumlyakov, I. Karaman, On the microstructural origins of martensitic transformation arrest in a NiCoMnIn magnetic shape memory alloy. *Acta Mater.* **142**, 95–106 (2018).
41. M. E. Manley, D. L. Abernathy, R. Sahul, D. E. Parshall, J. W. Lynn, A. D. Christianson, P. J. Stonaha, E. D. Specht, J. D. Budai, Giant electromechanical coupling of relaxor ferroelectrics controlled by polar nanoregion vibrations. *Sci. Adv.* **2**, e1501814 (2016).

42. G. Xu, Z. Zhong, Y. Bing, Z. G. Ye, G. Shirane, Electric-field-induced redistribution of polar nano-regions in a relaxor ferroelectric. *Nat. Mater.* **5**, 134–140 (2006).
43. R. Pirc, R. Blinc, V. S. Vikhnin, Effect of polar nanoregions on giant electrostriction and piezoelectricity in relaxor ferroelectrics. *Phys. Rev. B* **69**, 212105 (2004).
44. J. A. Fernandez-Baca, M. D. Lumsden, B. Winn, J. Zarestky, A. Zheludev, The triple-axis spectrometers at the high flux isotope reactor. *Neutron News* **19**, 18–21 (2008).
45. J. W. Lynn, Y. Chen, S. Chang, Y. Zhao, S. Chi, Ratcliff W 2nd, B. G. Ueland, R. W. Erwin, Double-focusing thermal triple-axis spectrometer at the NCNR. *J. Res. Natl. Inst. Stand. Technol.* **117**, 61–79 (2012).
46. D. L. Abernathy, M. B. Stone, M. J. Loguillo, M. S. Lucas, O. Delaire, X. Tang, J. Y. Y. Lin, B. Fultz, Design and operation of the wide angular-range chopper spectrometer ARCS at the Spallation Neutron Source. *Rev. Sci. Instrum.* **83**, 015114 (2012).
47. M. B. Stone, J. L. Niedziela, D. L. Abernathy, L. DeBeer-Schmitt, G. Ehlers, O. Garlea, G. E. Granroth, M. Graves-Brook, A. I. Kolesnikov, A. Podlesnyak, B. Winn, A comparison of four direct geometry time-of-flight spectrometers at the Spallation Neutron Source. *Rev. Sci. Instrum.* **85**, 045113 (2014).
48. J. Hlinka, S. Kamba, J. Petzelt, J. Kulda, C. A. Randall, S. J. Zhang, Origin of the "Waterfall" effect in phonon dispersion of relaxor perovskites. *Phys. Rev. Lett.* **91**, 107602 (2003).

Acknowledgments

Funding: This work was supported by the US Department of Energy, Office of Science, Office of Basic Energy Sciences, Materials Sciences and Engineering Division, under contract number DE-AC05-00OR22725. A portion of this research performed at the Oak Ridge National Laboratory's High Flux Isotope Reactor and Spallation Neutron Source was sponsored by the US Department of Energy, Office of Basic Energy Sciences. We acknowledge the support of the National Institute of Standards and Technology, US Department of Commerce, in providing the neutron research facilities used in this work. The identification of any commercial product or trade name does not imply endorsement or recommendation by the National Institute of Standards and Technology. I.K. and R.A. acknowledge the grant support from the US Army Research Office, grant no. W911NF2220117. **Author contributions:** M.E.M. and R.A. designed and planned this research. N.M.B., I.K., and Y.I.C. prepared the crystals. The triple-axis neutron measurements were performed by P.J.S. and M.E.M. with assistance from J.W.L. on BT7 at NIST and S.C. on HB3 at HFIR. The time-of-flight neutron measurements were performed by P.J.S. and M.E.M. with assistance from D.L.A. on ARCS at the SNS and M.B.S. on SEQUOIA at the SNS. Manuscript was written by M.E.M. with input from all authors. **Competing interests:** The authors declare that they have no competing interests. **Data and materials availability:** All data needed to evaluate the conclusions in the paper are present in the paper and/or the Supplementary Materials. Raw triple-axis neutron scattering data collected on the BT7 spectrometer are available at https://dx.doi.org/10.18434\T4201B?urlappend=bt7/201610/22757/ (magnetic field dependence) and https://dx.doi.org/10.18434/T4201B?urlappend=bt7/201511/20885/ (temperature dependence). Raw triple-axis neutron scattering data collected on the HB3 spectrometer are available at https://doi.org/10.14461/oncat.data/2337704 (temperature dependence). The data collected on the ARCS spectrometer are available at https://doi.org/10.14461/oncat.data/2333624 (MSMA) and https://doi.org/10.14461/oncat.data/2333625 (STG state). The data collected on the SEQUOIA spectrometer are located at https://doi.org/10.14461/oncat.data/2335305 (STG state).

Submitted 29 December 2023
Accepted 9 May 2024
Published 14 June 2024
10.1126/sciadv.adn2840